

Diagrammatic technique for simulation of large-scale quantum repeater networks with dissipating quantum memories

Viacheslav V. Kuzmin^{1,2} and Denis V. Vasilyev^{1,2}

¹*Center for Quantum Physics, University of Innsbruck, 6020 Innsbruck, Austria*

²*Institute for Quantum Optics and Quantum Information of the Austrian Academy of Sciences, 6020 Innsbruck, Austria*
(Dated: September 23, 2020)

We present a detailed description of the diagrammatic technique, recently devised in [V. V. Kuzmin *et. al.*, npj Quantum Information 5, 115 (2019)], for semi-analytical description of large-scale quantum-repeater networks. The technique takes into account all essential experimental imperfections, including dissipative Liouville dynamics of the network quantum memories and the classical communication delays. The results obtained with the semi-analytic method match the exact Monte Carlo simulations while the required computational resources scale only linearly with the network size. The presented approach opens new possibilities for the development and efficient optimization of future quantum networks.

I. INTRODUCTION

Quantum internet [1] aims at generating entangled states distributed over long distances, enabling such quantum technologies as secure communication [2], distributed quantum computing [3], and distributed metrology [4–7]. The major problem for implementation of a quantum internet is the exponential loss of photons — carriers of the entanglement — with the increasing length of the lossy channel. Quantum repeaters [8, 9] promise to overcome this problem. The idea is to split the distance between the network parties into elementary segments comparable with the fiber attenuation length, such that the high-fidelity entanglement in the segments could be distributed independently. The entangled states of the segments are generated probabilistically and are kept in quantum memories while others segments are under preparation. After that, the length of the entangled segments is extended using the quantum swapping operations [10] in a nested way [11].

Recent progress in quantum hardware gave rise to experimental implementation of individual components of the quantum repeater networks bringing closer realization of the first large-scale quantum internet. A non-exhaustive list of the experimental achievements includes: demonstration of generation of a distributed pair of entangled qubits [12–14]; long-coherence time, high efficiency and mode-multiplexing for quantum memories are separately presented in [15–25]; interfacing of atomic memories with telecom fiber [26–31]; swapping operation for qubits pairs [32–35]. The experimental progress leads to a theoretical challenge to analyze and optimize properties of real-world large-scale quantum networks taking into account all essential experimental imperfections.

The repeater networks subjected to such hardware imperfections as detectors inefficiency and dark counts, losses in fibers, classical communication delays, quantum memory read-out inefficiency, and memory decoherence were considered in a number of papers. In particular, the numerical and analytical study of quantum repeaters were presented in [9, 36–39]. These works, however, considered

simplified models for the quantum memory decoherence. For instance, in Ref. [36] the quantum memory efficiency is considered perfect until some finite coherence time t_{coh} after which the information is lost entirely. Authors of [9, 37] study effects of finite memory read-out efficiency in the limit of infinitely large memory coherence time. In Ref [39], a pure dephasing of memories and classical communication time in a one-dimensional (1D) repeater protocol were considered without other experimental imperfections.

The difficulty of modeling the protocols of quantum repeaters with a general time-continuous memory decoherence originates in the stochastic evolution of the networks. This evolution consists of random preparation of the elementary segments followed by probabilistic operations of entanglement swapping [11, 40]. A possible solution for exact simulation of such a probabilistic network is the Monte Carlo (MC) method, as was presented in Ref. [41–44]. Using this method one can recover statistics of a quantum network by simulating probabilistic trajectories, each of which represents execution of the full repeater protocol step by step. While being very flexible, the MC method has a limiting drawback — its runtime is proportional to the entanglement generation time in the simulated quantum network, which is quickly increasing with the network size. Therefore, the MC method becomes impractical for the performance evaluation and optimization of the real-world large-scale networks.

The purpose of the present paper is to elaborate on the alternative, semi-analytical, diagrammatic technique, which can be used to efficiently analyze the realistic quantum repeaters networks, as was demonstrated in our previous work [44]. This technique takes into account all essential experimental imperfections such as fiber losses, detectors losses, dark counts in detectors, memory read-out inefficiency, classical communication time, and the effect of dissipative Liouville dynamics on the network quantum memories (decay, dephasing, etc). The semi-analytical technique requires several orders of magnitude less computational run-time than the MC method while keeping the high precision of the simulation, as shown

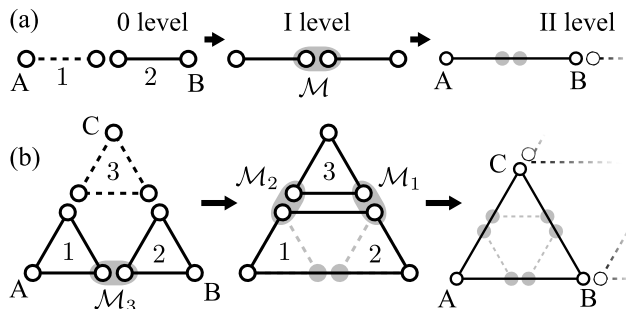


FIG. 1. Nesting level schemes of probabilistic quantum repeaters: (a) 1D repeater for the distribution of the Bell state $(|01\rangle + |10\rangle)/\sqrt{2}$ and (b) 2D repeater distributing the GHZ state $(|110\rangle + |001\rangle)/\sqrt{2}$. Circles represent quantum memories. Solid (dashed) lines indicate (dis-)entanglement of the connected memories. \mathcal{M} and \mathcal{M}_i are the superoperators representing merging operations applied to the pairs of quantum memories within the gray shaded areas. The gray colored quantum memories are traced out of the segments states.

below by direct comparison of the simulations results.

The paper is organized as follows. In Sec. II we introduce the repeater setup and explain the basic idea of the semi-analytic technique. Then we move on to develop the diagrammatic method step by step. In Sec. III A we introduce the elementary diagrams used in the semi-analytical method. In Sec. III B we derive basic equations for the 1D and 2D protocols which take into account imperfections in generation of the elementary repeater segments, imperfect merging operations, and the effect of dissipation on the network quantum memories. In Sec. IV we show how the diagrammatic technique incorporates the time for classical communications between the network nodes. In Sec. V we develop diagrams for describing the temporal filtering protocol [39, 44], which improves the fidelity of the states generated by the repeater networks in presence of finite memories time. In Sec. VI we benchmark the accuracy of the developed method against the MC simulation. Finally, in Sec. VII, we demonstrate a real-world application of the method — optimization of the network parameters for maximization of the secret key generation rate, and we conclude in Sec. VIII.

II. THE QUANTUM NETWORK SETUP AND THE SEMI-ANALYTIC METHOD

We start our discussion with a summary of the approach developed in [44] for analysis of the performance of large scale quantum repeater networks. A quantum network is a nested structure consisting of entangled nodes represented by quantum memories. Examples of one and two dimensional quantum networks are shown in the Fig. 1. The quantum repeater idea is to generate entanglement between the most remote nodes (circles in Fig. 1) of the network by probabilistic generation of entanglement between the adjacent nodes followed by a sequence of

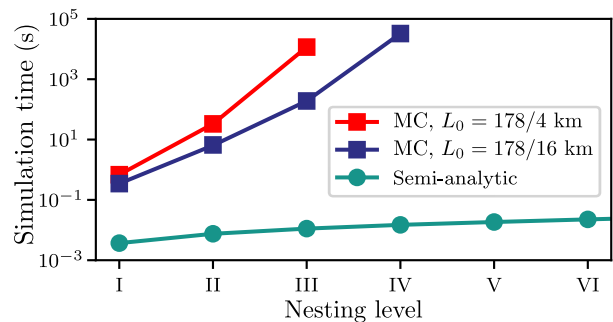


FIG. 2. Computation run time versus the network nesting level N . The physical distance covered by the network grows as $2^N L_0$ with L_0 the length of the elementary segment. Square points show the MC simulation run time required to achieve 1% standard deviation for the fidelity values. Red and blue colors show the two network sizes simulated by MC method: $L_0 = 178/16$ km and $L_0 = 178/4$ km. Round points show the computation time with the semi-analytical method, which does not depend on L_0 .

entanglement swapping operations. This allows to grow the size of the entangled segments (nodes connected by solid lines in Fig. 1) of the network until the most remote nodes become entangled.

On a more detailed level the quantum repeater protocol is described as follows. First, each elementary segment i , in the nesting level 0 of a network, is probabilistically prepared in an entangled state described by the density matrix ρ_i . The state is stored in quantum memories subjected to decoherence. Next, the neighboring segments of the network are probabilistically merged by applying the swapping operation to quantum memories within one node. Upon success, a larger number of nodes become entangled, thus, forming a network segment of the next nesting level. If the merging fails, the two segments have to be prepared again from scratch. The process is executed recursively until the final network state is prepared.

The challenge is to estimate performance of such a network in the presence of realistic imperfections such as photon loss, communication delay, quantum memory decay, etc. Here, we address the problem using the semi-analytic method devised in [44]. In this approach, unlike in the MC method, we derive analytical equations describing statistics of a single nesting level of the network. Thanks to the nested structure of the repeater protocol we recursively reuse the derived equations to evolve states of the elementary segments up to the final network level.

The main idea is to determine the density matrix distribution $\varrho(t)$ for the ensemble of states generated by the network at time t . More precisely, $\varrho(t)dt$ is the unnormalized density matrix of the ensemble of states generated within the time window $[t, t + dt)$, and $\text{Tr}\{\varrho(t)dt\}$ is the probability to generate the state within this time window. In the following we show how to obtain the Laplace image of the distribution, $\tilde{\varrho}(s) = \int_0^\infty e^{-st} \varrho(t) dt$, which fully describes the statistics of the network and allows one to infer the average generated state ρ and corresponding

generation time T :

$$\begin{aligned}\rho &= \int_0^\infty \varrho(t) dt = \tilde{\varrho}(s) \Big|_{s=0}, \\ T &= \int_0^\infty t \text{Tr} \{ \varrho(t) \} dt = -\text{Tr} \left\{ \frac{d\tilde{\varrho}(s)}{ds} \right\} \Big|_{s=0}.\end{aligned}\quad (1)$$

The method for deriving the equation for the density matrix distribution $\varrho(t)$ allows us to include a general time-continuous decoherence process which can be described by a Master Equation $\dot{\rho}_i = \mathcal{L}_i \rho_i$ with the Lindblad superoperator \mathcal{L}_i . The most time consuming part of the numerical calculation stage of the semi-analytical approach is solving a sparse system of linear equations involving the superoperator \mathcal{L}_i . This is a standard numerical problem which can be solved very efficiently. As a result we have a very fast method for simulation of quantum networks as shown in Fig. 2 [45]. The computation run-time grows only linearly with the number of nesting levels in the network and it is independent of the values of the network parameters. In contrast, the run-time for the MC simulation (implemented according to [44]) grows faster than exponential and depends on the elementary segment size L_0 , limiting the size of the simulated networks. Below, in Sec VI, we demonstrate that the results obtained by our approach match the MC simulation results.

The semi-analytical method involves summation of infinite series corresponding to averaging over all possible trajectories leading to generation of the final network state. Therefore, in the following Sections we introduce diagrams to facilitate the evaluation of the infinite sums representing density matrix distributions for quantum networks of high complexity.

III. DIAGRAMMATIC TECHNIQUE

In the section, we develop the diagrammatic technique for evaluation of the density matrix distribution describing merging of the network segments and, consequently, the full repeater protocol. First, we consider generation of the elementary segments, and then proceed with the description of the bipartite and tripartite networks based on the 1D and 2D repeater protocols, correspondingly.

A. Generation of elementary segments

First, we introduce diagrams representing generation of the elementary repeater segments (links in 1D case), which are the building blocks in the diagrammatic technique. Let us consider an elementary segment of a repeater network generated in discrete steps with success probability q for each attempt. We assume $q \ll 1$ (typical for quantum repeaters [11]) what results in a large number of

generation attempts $K \gg 1$. Then, the probability of generating the elementary segment in K attempts is

$$\begin{aligned}q_K &= q(1-q)^{K-1} \\ &= qe^{(K-1)\ln(1-q)} \approx qe^{-Kq}.\end{aligned}\quad (2)$$

Defining the time for one generation step as Δt , one can introduce an average link generation rate $\nu = q/\Delta t$, total link generation time $t = K\Delta t$, and the continuous probability distribution

$$p(t) = \nu e^{-\nu t}, \quad (3)$$

with the Laplace image

$$\tilde{p}(s) = \frac{\nu}{s + \nu}. \quad (4)$$

Now, we introduce the elementary diagram representing the density matrix distribution for generation of a segment i in the state ρ_i at time t :

$$\varrho_i(t) = p(t)\rho_i = \nu e^{-\nu t} \rho_i \equiv \begin{array}{c} \bullet \\ | \\ 0 \end{array}. \quad (5)$$

Here the vertical line of length t represents the total link generation time, and the circle denotes the successful generation event. Time flows upward.

B. 1D repeater

Consider a 1D repeater network consisting of two links with states ρ_1 and ρ_2 generated at the rate ν , as shown in Fig. 1(a). The goal is to find the average state ρ and the generation time T of the segment in the next nesting level obtained by merging the two links. After that, we can define a recursive procedure to find average states generated at all nesting levels of the network.

Generation of segments within one nesting level. We proceed starting with the density matrix distribution for generating the i^{th} link in state ρ_i before the j^{th} link has been generated at time t in state ρ_j which can be constructed using two diagrams (5),

$$\begin{aligned}\varrho_{ij}(t) &= \begin{array}{c} \vdots \\ \bullet \\ | \\ t' \\ | \\ 0 \end{array} \\ &= p(t) \int_0^t dt' p(t') e^{(t-t')\mathcal{L}_i} \rho_{\text{in}} \equiv X_{ij}(t) \rho_{\text{in}},\end{aligned}\quad (6)$$

with $\rho_{\text{in}} = \rho_1 \otimes \rho_2$. Here we introduce propagator $X_{ij}(t)$ which includes integration over all intermediate times t' of the i^{th} link creation. The degradation of the i^{th} link during the waiting time $t - t'$ due to the finite lifetime of the quantum memory is represented by the dashed line and is taken into account using the Lindblad superoperator \mathcal{L}_i [46]. Inserting the probability distributions (3) into

Eq. (6) we find the Laplace image of the density matrix distribution $\tilde{\varrho}_{ij}(s) = \tilde{X}_{ij}(s)\rho_{\text{in}}$ with

$$\begin{aligned} \tilde{X}_{ij}(s) &= \int_0^\infty dt e^{-st} X_{ij}(t) \\ &= \nu^2 \int_0^\infty dt e^{-(s+\nu)t} \int_0^t dt' e^{-\nu t'} e^{(t-t')\mathcal{L}_i} \\ &= \frac{\nu^2}{(s'+\nu)(s'-\mathcal{L}_i)} \Big|_{s'=s+\nu}. \end{aligned} \quad (7)$$

Here we use the fact that the convolution of two functions in Eq. (6) is transformed into a product of their Laplace images and the exponential prefactor shifts the frequency of the Laplace images.

Summing over two possible orders of the segments generation $(i, j) = \{(1, 2), (2, 1)\}$ we obtain the density matrix distribution and its Laplace image for the two segments prepared for merging at time t ,

$$\varrho_{\text{prep}}(t) = \sum_{ij} \varrho_{ij}(t) = \begin{array}{c} \vdots \\ | \\ t_0 \\ | \\ \vdots \end{array} \begin{array}{c} t \\ | \\ \vdots \end{array} + \begin{array}{c} \vdots \\ | \\ t \\ | \\ \vdots \end{array} \begin{array}{c} t_0 \\ | \\ \vdots \end{array}, \quad (8)$$

$$\begin{aligned} \tilde{\varrho}_{\text{prep}}(s) &= \sum_{ij} \tilde{\varrho}_{ij}(s) = \sum_{ij} \tilde{X}_{ij}(s)\rho_{\text{in}} \\ &= \frac{\nu^2}{(s'+\nu)} \left[\frac{1}{(s'-\mathcal{L}_1)} + \frac{1}{(s'-\mathcal{L}_2)} \right] \Big|_{s'=s+\nu} \rho_{\text{in}}. \end{aligned} \quad (9)$$

Merging of the generated segments. Once both segments are prepared, we perform a probabilistic merging operation described by a non-trace-preserving superoperator \mathcal{M} (see Appendix A). A successful merging of the two prepared segments with *one* attempt at time t results in the longer segment with the density matrix distribution given by

$$\mathcal{M}\varrho_{\text{prep}}(t) \equiv \begin{array}{c} \vdots \\ | \\ t \\ | \\ \vdots \end{array} + \begin{array}{c} t \\ | \\ \vdots \\ | \\ t_0 \\ | \\ \vdots \end{array} \equiv \begin{array}{c} \vdots \\ | \\ t \\ | \\ \vdots \end{array}, \quad (10)$$

here we introduce a new diagram to represent the merging result. The probability density for a failed merging operation at time t reads

$$\text{Tr}\{(\mathcal{I} - \mathcal{M})\varrho_{\text{prep}}(t)\} \equiv \begin{array}{c} \vdots \\ | \\ t \\ | \\ \vdots \end{array}, \quad (11)$$

where \mathcal{I} is the unit superoperator. Next, a diagram describing a successful merging at time t with one failed attempt at time t_0 is constructed out of diagrams (10) and (11) as,

$$\begin{array}{c} \vdots \\ | \\ t \\ | \\ \vdots \end{array} = \int_0^t dt_0 \mathcal{M}\varrho_{\text{prep}}(t) \cdot \text{Tr}\{(\mathcal{I} - \mathcal{M})\varrho_{\text{prep}}(t_0)\}, \quad (12)$$

where we integrate over all possible times of the failed attempt $0 < t_0 < t$. Distribution (12) is a convolution and its Laplace image is a product of the Laplace images of Eqs. (10) and (11), $\mathcal{M}\tilde{\varrho}_{\text{prep}}(s) \cdot \text{Tr}\{(\mathcal{I} - \mathcal{M})\tilde{\varrho}_{\text{prep}}(s)\}$.

Sum over all trajectories. The target density matrix distribution $\varrho(t)$ of the longer segment is obtained by summing over all possible combinations of unsuccessful mergings leading to a final successful generation of an entangled state

$$\varrho(t) = \begin{array}{c} \vdots \\ | \\ t \\ | \\ \vdots \end{array} + \begin{array}{c} \vdots \\ | \\ t \\ | \\ t_0 \\ | \\ \vdots \end{array} + \begin{array}{c} \vdots \\ | \\ t \\ | \\ t_1 \\ | \\ t_0 \\ | \\ \vdots \end{array} + \dots \quad (13)$$

In the Laplace domain, the sum (13) corresponds to a geometric series, which converges to

$$\begin{aligned} \tilde{\varrho}(s) &= \mathcal{M}\tilde{\varrho}_{\text{prep}}(s) \sum_{m=0}^{\infty} [\text{Tr}\{(\mathcal{I} - \mathcal{M})\tilde{\varrho}_{\text{prep}}(s)\}]^m \\ &= \frac{\mathcal{M}\tilde{\varrho}_{\text{prep}}(s)}{1 - \text{Tr}\{(\mathcal{I} - \mathcal{M})\tilde{\varrho}_{\text{prep}}(s)\}}. \end{aligned} \quad (14)$$

Finally, inserting Eq. (9) into Eq. (14) and taking into account that $\text{Tr}\{\mathcal{L}_i\rho_i\} = 0$, we use Eq. (1) to obtain the average state and generation time

$$\begin{aligned} \rho &= \tilde{\varrho}(s) \Big|_{s=0} = \frac{\mathcal{M}\tilde{\varrho}_{\text{prep}}(0)}{\text{Tr}\{\mathcal{M}\tilde{\varrho}_{\text{prep}}(0)\}} \\ &= \frac{1}{P} \cdot \frac{1}{2} \mathcal{M} \left(\frac{1}{1 - \mathcal{L}_1/\nu} + \frac{1}{1 - \mathcal{L}_2/\nu} \right) \rho_1 \otimes \rho_2 \quad (15) \\ T &= -\text{Tr} \left\{ \frac{d\tilde{\varrho}(s)}{ds} \right\} \Big|_{s=0} = \frac{1}{P} \cdot \frac{3}{2\nu}, \end{aligned}$$

with $P = \text{Tr}\{\mathcal{M}\tilde{\varrho}_{\text{prep}}(0)\}$ the average merging probability. One can see that the probability of the eventual state preparation $\text{Tr}\{\rho\} = 1$. This indicates that we take into account all possible trajectories. The resulting Eqs. (15) allow us to find the state and the generation time of the next nesting level segment using efficient numerical algorithms for solving the sparse systems of linear equations involving \mathcal{L}_i .

Full repeater protocol. To address the next nesting level of the network, we assume that its segments are generated time-independently in states $\rho'_i \equiv \rho$ with rates $\nu' \equiv 1/T$ obtained from Eqs. (15). In other words, we assume that the generation of the segments in the next network levels is a Poissonian process, and Eqs. (9) and (15) can be reused to evaluate the properties of the higher nesting levels segments. This is an approximation since the exact density matrix distribution $\varrho(t)$ given by its Laplace image (14) describes preparation of states which

are time-dependent. This is, however, a very good approximation as we show below.

Using the described procedure recursively, we can find states and generation times of all nesting levels of the network. Notice, that Eqs. (9) and (15) operate with a quantum state of at most 4 quantum memories, therefore, the calculation of the desired quantities does not demand a lot of computational resources in comparison with the MC method.

Finally, we mention that to start the described recursion, one has to obtain states $\{\rho_i\}$ and generation rate $\nu = q/\Delta t$ of the elementary segments, and compute the merging superoperator \mathcal{M} . To obtain $\{\rho_i\}$, q and Δt one can simulate the protocol for preparation of the elementary segment, for example, in terms of density matrices taking into account all essential experimental imperfections. Superoperator \mathcal{M} is calculated based on the merging protocol taking into account the imperfections as well. An example of simulation of the elementary segments and construction of \mathcal{M} for the DLCZ protocol is presented in Appendix A.

Verification of the approximations validity. In the following, we illustrate the validity of the approximation of regarding the generation of the segments in the next network levels as a Poissonian process. We consider the case of no dissipation, $\mathcal{L}_i = 0$, and compare the exact generation probability distribution $r(t) = \text{Tr}\{\varrho(t)\}$ for the segment generated in the first nesting level with the Poissonian distribution of rate $1/T$ defined in Eqs. (15).

First, we obtain the Laplace image of $r(t)$ as $\tilde{r}(s) = \text{Tr}\{\tilde{\varrho}(s)\}$. From Eq. (9), in the case of $\mathcal{L}_i = 0$, we obtain

$$\begin{aligned} \text{Tr}\{\mathcal{M}\tilde{\varrho}_{\text{prep}}(s)\} &= P \cdot \text{Tr}\{\tilde{\varrho}_{\text{prep}}(s)\} \\ \text{Tr}\{\tilde{\varrho}_{\text{prep}}(s)\} &= \frac{2\nu^2}{(s+2\nu)(s+\nu)} \end{aligned}$$

Then, using the above equations and Eq. (14), one can obtain

$$\tilde{r}(s) = \frac{2P\nu^2}{s^2 + 3\nu s + 2P\nu^2}. \quad (16)$$

This function has two poles in the left half-plane at points $3\nu(-1 \pm \sqrt{1 - (8/9)P})/2$, each of which, in the time domain, corresponds to an additive exponential term with the decay rate given by the pole. In the limit of small merging success probability, $P \ll 1$, the first-order Taylor expansion reveals that one pole $a \approx -3\nu + (2/3)P\nu$ gives an exponent decaying much faster than the exponent arising from the second pole $b \approx -(2/3)P\nu$. As a result, we obtain the probability distribution as

$$\begin{aligned} r(t) &= 2P\nu^2 \frac{1}{a-b} (e^{at} - e^{bt}) \\ &\xrightarrow{P \ll 1, \nu t \gg 1} \frac{2}{3} P\nu e^{-\frac{2}{3}P\nu t} = \frac{1}{T} e^{-\frac{t}{T}} \end{aligned}$$

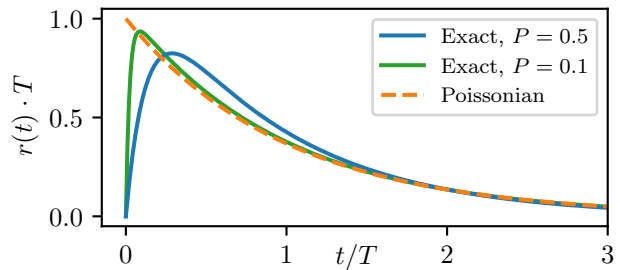


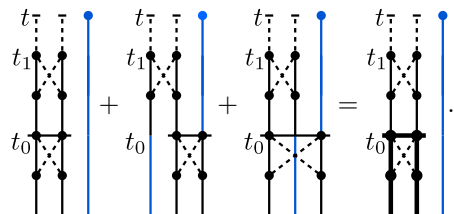
FIG. 3. Exact distributions to generate a state of the first nesting level for various probabilities for the merging success P and their approximation by the Poissonian distribution. T is the average generation time from Eqs. (15).

with the asymptotic behavior approaching the Poissonian distribution with rate $1/T$, where T is defined by Eqs. (15). This behavior is demonstrated in Fig. 3 for $P = 0.5$ and $P = 0.1$. For realistic networks this approximation is fulfilled well since the merging probability is at most 0.5 for an ideal setup and drops quickly with the addition of realistic imperfections and increase of the nesting level of the network.

C. 2D repeater

In the subsection, we develop the diagrammatic technique for the protocol of the 2D repeater illustrated in Fig. 1(b). The 2D repeater is implemented in a nested way, such that, at each nesting level, segments $i = \{1, 2, 3\}$ with states ρ_i and generation rates ν are probabilistically merged to form the segment of the next nesting level with the state ρ . The segments are generated in random order ijk , which is one of the possible permutations of the segments indices $\{123\}$. Merging of the first pair of prepared segments, i and j , is described by the superoperator \mathcal{M}_k (see Appendix A). Merging of the resulting four-node state with the third prepared segment k is implemented with two merging operations \mathcal{M}_i and \mathcal{M}_j , which can be combined in one superoperator $\mathcal{M}_k \equiv \mathcal{M}_i \mathcal{M}_j$.

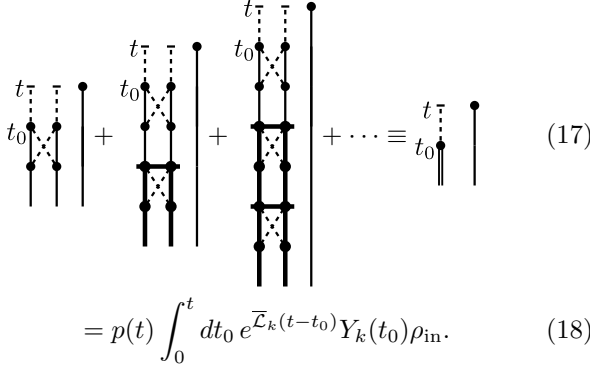
Now we show how to find the density matrix distributions for the 2D repeater protocol reusing some of the results obtained for the 1D repeater in the previous section. First, let us consider the following equality for diagrams describing a set of trajectories for 3 segments of the 2D repeater including one successful and one unsuccessful attempts to merge two segments



The diagrams in the left part of the equality illustrate all 6 possible variants for a failed merging of a pair of

segments at time t_0 followed by a successful merging of a pair of segments (prepared in two possible orders). Then, the successfully merged at time t_1 state degrades until the third segment is generated at time t . In the diagrams, each vertical line of some length t' represents probability that a segment, being generated with the rate ν , is not prepared at the time t' and, in time domain, gives a prefactor $\exp(-\nu t')$ to the density matrix distribution. Therefore, two such vertical lines of length t'_1 and t'_2 can be combined in a single line of length $t'_1 + t'_2$. Thus, in the left part of the equality, we can reshuffle parts of the diagrams to collect the blue colored lines a single column. This can be done if the segments have identical generation rates ν . Afterward, the parts of the diagrams corresponding to the failed mergings can be factored out and summed to a new diagram which we illustrated with bold lines. In the following we omit the blue color of the line.

Now we can represent all possible trajectories for merging of two segments $i, j \neq k$ at time t as



$$= p(t) \int_0^t dt_0 e^{-\bar{\mathcal{L}}_k(t-t_0)} Y_k(t_0) \rho_{\text{in}}. \quad (18)$$

with $\rho_{\text{in}} = \rho_1 \otimes \rho_2 \otimes \rho_3$. Here $p(t)$ given by Eq. (5) is the probability distribution for generation of the last prepared segment k . Propagator $Y_k(t)$ generates a merged state of segment $i, j \neq k$ at time t_0 averaged over all possible trajectories, and superoperator $\bar{\mathcal{L}}_k$ describes degradation of segments i and j after their merging. The Laplace image of Eq. (18) is

$$\frac{\nu}{s' - \bar{\mathcal{L}}_k} \tilde{Y}_k(s') \Big|_{s'=s+\nu} \rho_{\text{in}}. \quad (19)$$

Here $\tilde{Y}_k(s')$ is the Laplace image of $Y_k(t)$, which can be obtained in analogy to Eq. (14) by summing a geometric series of diagrams with all possible variants of the failed mergings

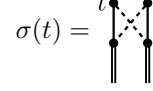
$$\tilde{Y}_k(s) = \frac{\mathcal{M}_k}{1 - \tilde{p}_{\text{fail}}^{(1)}(s)} \left[\tilde{X}_{ij}(s) + \tilde{X}_{ji}(s) \right], \quad i, j \neq k,$$

In the above equation, $\tilde{X}_{ij}(s)$ and $\tilde{X}_{ji}(s)$ given by Eq. (7) describe two orders of generation of the merged segments i and j . At the same time, the Laplace image $\tilde{p}_{\text{fail}}^{(1)}(s)$ of the probability distribution for a failed merging includes

all 6 possible generation orders $\{ijk\}$ which can lead to a failed merging

$$\begin{aligned} \tilde{p}_{\text{fail}}^{(1)}(s) = \text{Tr} \Big\{ & ([\mathcal{I} - \mathcal{M}_1][\tilde{X}_{23}(s) + \tilde{X}_{32}(s)] \\ & + [\mathcal{I} - \mathcal{M}_2][\tilde{X}_{13}(s) + \tilde{X}_{31}(s)] \\ & + [\mathcal{I} - \mathcal{M}_3][\tilde{X}_{12}(s) + \tilde{X}_{21}(s)]) \rho_{\text{in}} \Big\}. \end{aligned}$$

The diagram for a successful attempt of the third, last, merging is represented as

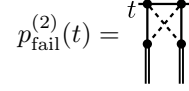


$$\sigma(t) =$$

and includes three possible variants with one of three segments $k \in \{1, 2, 3\}$ being prepared at the end. In analogy with Eq. (10), we use Laplace image (19) for diagram (17) to find the Laplace image of $\sigma(t)$ as

$$\tilde{\sigma}(s) = \sum_{k=\{1,2,3\}} \bar{\mathcal{M}}_k \frac{\nu}{s' - \bar{\mathcal{L}}_k} \tilde{Y}_k(s') \Big|_{s'=s+\nu} \rho_{\text{in}}.$$

The diagram for the corresponding failed merging is

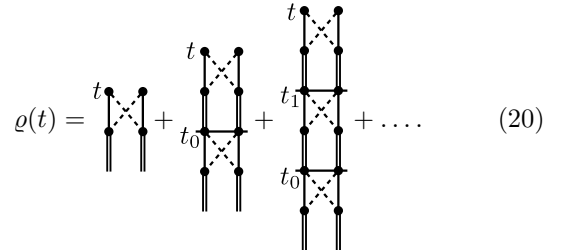


$$p_{\text{fail}}^{(2)}(t) =$$

with the Laplace image obtained by replacing $\bar{\mathcal{M}}_k$ with $I - \bar{\mathcal{M}}_k$ in the equation for $\tilde{\sigma}(s)$ and taking its trace

$$\begin{aligned} \tilde{p}_{\text{fail}}^{(2)}(s) = \sum_{k=\{1,2,3\}} \text{Tr} \Big\{ & (I - \bar{\mathcal{M}}_k) \frac{\nu}{s' - \bar{\mathcal{L}}_k} \\ & \times \tilde{Y}_k(s') \Big|_{s'=s+\nu} \rho_{\text{in}} \Big\}. \end{aligned}$$

Then, similar to diagrams series (13), the distribution for the final state preparation can be written as an infinite sum



$$\varrho(t) =$$

The diagrams in Eq. (20) becomes a geometric series in the Laplace domain and its sum equals to

$$\tilde{\varrho}(s) = \frac{\tilde{\sigma}(s)}{1 - p_{\text{fail}}^{(2)}(s)}. \quad (21)$$

Introducing the average success probability for the first merging as $P_1 = 1 - \tilde{p}_{\text{fail}}^{(1)}(0)$ and for the combination of the second and the third mergings as $P_2 = 1 - \tilde{p}_{\text{fail}}^{(2)}(0)$ one can find using Eqs. (1) the average state and generation time as

$$\begin{aligned} \rho &= \tilde{\varrho}(s) \Big|_{s=0} = \frac{1}{6P_1P_2} \sum_{k=\{1,2,3\}} \bar{\mathcal{M}}_k \frac{1}{1 - \bar{\mathcal{L}}_k/\nu} \\ &\times \mathcal{M}_k \sum_{i \neq k} \frac{1}{1 - \mathcal{L}_i/(2\nu)} \rho_{\text{in}}, \\ T &= -\text{Tr} \left\{ \frac{d\tilde{\varrho}(s)}{ds} \right\} \Big|_{s=0} = \frac{5}{6P_1P_2\nu}. \end{aligned} \quad (22)$$

In analogy with the 1D repeater, here we demonstrate that the next-nesting-level network can be calculated using the same Eq. (22) with the input given by the average density matrix ρ and the average generation rate $1/T$ obtained for the current nesting level. To do that, we consider probability distribution $r(t)$ for generation of a segment in the first nesting level in the case with no decoherence, $\mathcal{L}_k = 0$ and $\bar{\mathcal{L}}_k = 0$ and compare it with the Poissonian distribution. Under this simplification, the Laplace image of the distribution $\tilde{r}(s) = \text{Tr}\{\tilde{\varrho}(s)\}$ can be obtained by replacing in the above equations all the merging superoperators to the average merging probabilities, $\mathcal{M}_k \rightarrow P_1$ and $\bar{\mathcal{M}}_k \rightarrow P_2$, and then taking the trace. As a result, one can find

$$\tilde{r}(s) = \frac{6P_1P_2\nu^3}{s^3 + 6s^2\nu + (5 + 6P_1)s\nu^2 + 6P_1P_2\nu^3}. \quad (23)$$

This function has three poles, which in the limit of small merging success probabilities, $P_1, P_2 \ll 1$, have the dominating parts $-6/5P_1P_2\nu$, -5ν , and $-\nu$. In the time domain, the first pole results in an exponent which has the slowest decay rate and, therefore, gives the asymptotic behavior of the probability distribution

$$r(t) \Big|_{P_1, P_2 \ll 1, \nu t \gg 1} \rightarrow \frac{6}{5} P_1 P_2 \nu e^{-\frac{6}{5} P_1 P_2 \nu t} = \frac{1}{T} e^{-\frac{t}{T}}$$

which approaches the Poissonian distribution with rate $1/T$ for $t\nu \gg 1$ with T given by Eqs. (22). The validity of this approximation for the case with dissipation, $\mathcal{L}_k \neq 0$ and $\bar{\mathcal{L}}_k \neq 0$, will be demonstrated in Sec. VI by comparing the results obtained with the diagrammatic technique and the data simulated with the Monte Carlo method. The 2D repeater protocol with the communication time and the temporal filtering protocol is detailed in Appendix B

IV. COMMUNICATION TIME

In the following section, we incorporate classical communication time into the diagrammatic technique. For demonstration, we do so for the 1D repeater scheme,

which is studied in Sec. III. The communication time for the 2D repeater protocol is given in Appendix B.

To include the communication time, we take into account that after each merging attempt, one needs time $t_m = t_{\text{swap}} + t_c$ in order to continue the generation. Here t_{swap} is the time required for a swapping operation, and t_c is the time required for the classical communication between nodes of the segment of current nesting level N and which scales as $t_c \propto 2^N$. We assume that the communication time t_c is identical for all segments $\{i\}$ at one nesting level. The communication time does not affect diagrams for the segments generation introduced in Sec. III B and only changes the diagrams for the merging.

Merging of generated segments. An extra waiting time t_m after a merging operation leads to an additional memory decoherence $\exp\{\mathcal{L}t_m\}$ of the generated state with the Lindblad superoperator \mathcal{L} . The waiting time is incorporated into the diagrammatic technique by modifying the diagram (10) which represents a successful merging:

$$\begin{aligned} &\text{Diagram: } \left[\begin{array}{c} \text{---} \\ \text{---} \\ \text{---} \\ \text{---} \end{array} \right] \xrightarrow{t} \left[\begin{array}{c} \text{---} \\ \text{---} \\ \text{---} \\ \text{---} \end{array} \right] \xrightarrow{t-t_m} \left[\begin{array}{c} \text{---} \\ \text{---} \\ \text{---} \\ \text{---} \end{array} \right] \\ &= \Theta(t - t_m) e^{\mathcal{L}t_m} \mathcal{M} \varrho_{\text{prep}}(t - t_m), \end{aligned} \quad (24)$$

where $\varrho_{\text{prep}}(t)$ is the density matrix distribution (8) of the two segments prepared for merging. Here the delay t_m is represented by the Heaviside function $\Theta(t - t_m)$ since there is zero probability to communicate about the merged state if $t < t_m$. The Laplace image of the distribution (24) is $\exp\{-st_m\} \exp\{\mathcal{L}t_m\} \mathcal{M} \tilde{\varrho}_{\text{prep}}(s)$, where $\tilde{\varrho}_{\text{prep}}(s)$ is defined by Eq. (9). The Heaviside function in the diagram (24) results in the extra exponent prefactor. In a similar way, a failed merging is described by the modified diagram (11) as

$$\begin{aligned} &\text{Diagram: } \left[\begin{array}{c} \text{---} \\ \text{---} \\ \text{---} \\ \text{---} \end{array} \right] \xrightarrow{t} \left[\begin{array}{c} \text{---} \\ \text{---} \\ \text{---} \\ \text{---} \end{array} \right] \\ &= \Theta(t - t_m) \text{Tr} \{ (\mathcal{I} - \mathcal{M}) \varrho_{\text{prep}}(t - t_m) \}, \end{aligned}$$

with the Laplace image $\exp\{-st_m\} \text{Tr} \{ (\mathcal{I} - \mathcal{M}) \tilde{\varrho}_{\text{prep}}(s) \}$. Here we took into account that \mathcal{L} is the trace-preserving operator.

Sum over all trajectories. The final density matrix distribution is an infinite sum

$$\varrho(t) = \left[\begin{array}{c} \text{---} \\ \text{---} \\ \text{---} \\ \text{---} \end{array} \right] \xrightarrow{t} \left[\begin{array}{c} \text{---} \\ \text{---} \\ \text{---} \\ \text{---} \end{array} \right] \xrightarrow{t_0} \left[\begin{array}{c} \text{---} \\ \text{---} \\ \text{---} \\ \text{---} \end{array} \right] \xrightarrow{t_1} \left[\begin{array}{c} \text{---} \\ \text{---} \\ \text{---} \\ \text{---} \end{array} \right] + \dots,$$

which in the Laplace domain converges to

$$\tilde{\varrho}(s) = \frac{e^{\mathcal{L}t_m} \mathcal{M} \tilde{\varrho}_{\text{prep}}(s)}{e^{st_m} - \text{Tr} \{ (\mathcal{I} - \mathcal{M}) \tilde{\varrho}_{\text{prep}}(s) \}}. \quad (25)$$

Inserting image (25) to Eqs. (1) we obtain the average network state and generation time

$$\begin{aligned} \rho &= \tilde{\varrho}(s) \Big|_{s=0} = \frac{1}{P} e^{\mathcal{L}t_m} \mathcal{M} \tilde{\varrho}_{\text{prep}}(0) \\ T &= -\text{Tr} \left\{ \frac{d\tilde{\varrho}(s)}{ds} \right\} \Big|_{s=0} = \frac{1}{P} \left(t_m + \frac{3}{2\nu} \right), \end{aligned} \quad (26)$$

where $P = \text{Tr} \{ \mathcal{M} \tilde{\varrho}_{\text{prep}}(0) \}$ is the average merging probability and $\tilde{\varrho}_{\text{prep}}(s)$ is defined by Eq. (9). In comparison with Eqs. (15), where the communication time is not included, Eqs. (26) take into account the extra decoherence of the generated state for time t_m and include t_m to each cycle of the segment preparation and merging.

V. TEMPORAL FILTERING PROTOCOL

In the section, we develop the diagrammatic technique for the temporal filtering protocol [44]. The temporal filtering protocol allows one to significantly improve the quality of the entangled states distributed by the quantum repeaters in the presence of finite memory times. The idea of the protocol is to discard the state of a prepared repeater segment as it becomes older than a certain filtering time τ . After the communication time t_c , the preparation of the discarded state is restarted. Although discarding of the prepared states increases the overall generation time, the protocol suppresses the effect of the memory decoherence on the final average state generated by the network.

In fact, the temporal filtering protocol can be considered as the general case of the repeater protocol [8] and the so-called ‘‘quantum relay’’ protocol [47]. In the original quantum repeater protocol, the memory time is required to be much longer than the time for the state generation, and, therefore, the temporal filtering is not required, i.e., filtering time $\tau \rightarrow \infty$. In the memory-less quantum relay protocol, all segments states have to be generated simultaneously, otherwise the prepared states are discarded, i.e., $\tau \rightarrow 0$. In contrast to these two extreme cases, the temporal filtering protocol allows a quantum network to optimally exploit realistic finite memory coherence times by using a finite nonzero τ .

Previously, the protocol for re-preparation of the longly decaying states in 1D repeater was considered in Refs. [36, 39, 44]. In Ref. [36], the segments memories stay unaffected for the memory time τ , and afterward, the segments states are re-generated. In Ref. [39], filtration of the segments states was studied for the 1D repeater with quantum memories subjected to dephasing. The protocol considered in Ref. [39] also demands that the prepared segments can be used only at discrete moments of time, therefore, requiring that the generated

segments experience extra unnecessary decoherence while waiting for this time moments. In the following, we develop the diagrammatic technique which allows us to consider the temporal filtering protocol for any dissipative Liouville dynamics of memories, and which can be used in various repeater-network architectures being free of the mentioned unnecessary waiting time presented in method [39]. Particularly, in our previous work [44], the developed approach was used for the 2D repeater scheme with the decaying memories.

For illustration, in this section, we describe the diagrammatic technique incorporating the temporal filtering in the 1D repeater model taking into account the communication time considered in the previous section. The temporal filtering does not change the diagrams for the merging with communication time, it affects only the diagrams for the segments preparation. The temporal filtering protocol for the 2D repeater scheme is given in Appendix B.

Generation of segments within one nesting level. In the following we introduce a new diagram representing preparation of two segments at time t within the time window $[\max\{t - \tau, 0\}, t]$. There are two possible cases: $t < \tau$ and $t \geq \tau$ which we sum up as following

$$\begin{aligned} \left. \begin{array}{c} \vdots \\ \vdots \\ \bullet \\ \vdots \\ \vdots \end{array} \right\} t &= \left. \begin{array}{c} \vdots \\ \vdots \\ \bullet \\ \vdots \\ \vdots \end{array} \right\} t_0 \left. \begin{array}{c} \vdots \\ \vdots \\ \bullet \\ \vdots \\ \vdots \end{array} \right\} \tau + \left. \begin{array}{c} \vdots \\ \vdots \\ \bullet \\ \vdots \\ \vdots \end{array} \right\} \tau \\ &= \left[\Theta(\tau - t) \int_0^t \bullet dt_0 + \Theta(t - \tau) \int_{t-\tau}^t \bullet dt_0 \right] \\ &\quad \times p(t) p(t_0) e^{\mathcal{L}_i(t-t_0)} \cdot \rho_{\text{in}}, \end{aligned} \quad (27)$$

where we use superoperator notation such that the function after the square brackets is inserted in place of the bullets. Notice that, in the second diagram of the sum, with $t \geq \tau$, the integration over t_0 is done only within the filtering time τ preceding the time moment t . The diagram representing two possible orders for the successful generation of two links with no filtration is

$$\varrho_{\text{nf}}(t) = \left. \begin{array}{c} \vdots \\ \vdots \\ \bullet \\ \vdots \\ \vdots \end{array} \right\} t_0 \left. \begin{array}{c} \vdots \\ \vdots \\ \bullet \\ \vdots \\ \vdots \end{array} \right\} t + \left. \begin{array}{c} \vdots \\ \vdots \\ \bullet \\ \vdots \\ \vdots \end{array} \right\} t \left. \begin{array}{c} \vdots \\ \vdots \\ \bullet \\ \vdots \\ \vdots \end{array} \right\} t_0 \equiv \left. \begin{array}{c} \vdots \\ \vdots \\ \bullet \\ \vdots \\ \vdots \end{array} \right\} t \left. \begin{array}{c} \vdots \\ \vdots \\ \bullet \\ \vdots \\ \vdots \end{array} \right\} t. \quad (28)$$

After inserting the generation probability distribution (3) into Eq. (27) one can obtain the Laplace image for Eq. (28) as

$$\begin{aligned} \tilde{\varrho}_{\text{nf}}(s) &= \sum_{ij} \left(1 - e^{-(s' - \mathcal{L}_i)\tau} \right) \\ &\quad \times \frac{\nu^2}{(s' - \mathcal{L}_i)(s' + \nu)} \rho_{\text{in}} \Big|_{s'=s+\nu}. \end{aligned} \quad (29)$$

Now we introduce a diagram representing the probability density to filter out a segment state of age τ at time t

if the second segment is not generated

$$\begin{aligned} \tau &= \Theta(t - \tau - t_c) e^{-\nu(t-t_c)} p(t - \tau - t_c) \\ &= \Theta(t - \tau - t_c) \nu e^{-\nu(2t-2t_c-\tau)}, \end{aligned} \quad (30)$$

with $p(t)$ given in (3). This diagram is constructed out of the diagram (5) describing a successful generation of a segment at time $t - \tau - t_c$ and a vertical line of length $t - t_c$ representing the unsuccessful attempts to prepare the second segment during time $t - t_c$. In the diagram (30), we take into account that, as the segment is discarded, the communication time t_c is required to inform the nearby nodes that the link has to be regenerated as it grew too “old”. Here, we neglect a small probability $1 - \exp(-\nu t_c) \approx \nu t_c$, that the unprepared link can be generated within the communication time $t_c \ll 1/\nu$, and, therefore, in the diagram, its generation is also stopped for the communication time t_c . This assumption is required in order to sum up the diagram series, and it only slightly overestimates the effect of the communication time. This will be verified below by benchmarking against the MC method.

The probability distribution for the two possible events of the segments filtration is represented by the following diagram

$$p_f(t) = \begin{array}{c} \text{---} t \\ | \\ \bullet \\ | \\ \text{---} t_c \\ | \\ \bullet \\ | \\ \text{---} \tau \\ | \\ \bullet \\ | \\ \text{---} t \end{array} + \begin{array}{c} \text{---} t \\ | \\ \bullet \\ | \\ \text{---} t_c \\ | \\ \bullet \\ | \\ \text{---} \tau \\ | \\ \bullet \\ | \\ \text{---} t \end{array} \equiv \begin{array}{c} \text{---} t \\ | \\ \bullet \\ | \\ \text{---} t \\ | \\ \bullet \\ | \\ \text{---} t \end{array} \quad (31)$$

with the Laplace image obtained from Eq. (30) as

$$\tilde{p}_f(s) = 2e^{-s(\tau+t_c)} \frac{\nu e^{-\nu\tau}}{s + 2\nu}. \quad (32)$$

Using diagrams (28) and (31) we obtain the density matrix distribution for the two segments prepared to be merged:

$$\varrho_{\text{prep}}(t) = \begin{array}{c} \text{---} t \\ | \\ \bullet \\ | \\ \text{---} t \end{array} + \begin{array}{c} \text{---} t \\ | \\ \bullet \\ | \\ \text{---} t_0 \\ | \\ \bullet \\ | \\ \text{---} t_0 \end{array} + \begin{array}{c} \text{---} t \\ | \\ \bullet \\ | \\ \text{---} t_1 \\ | \\ \bullet \\ | \\ \text{---} t_1 \end{array} + \dots, \quad (33)$$

which, in the Laplace domain, reads

$$\tilde{\varrho}_{\text{prep}}(s) = \sum_{n=0}^{\infty} \tilde{\varrho}_{\text{nf}}(s) [\tilde{p}_f(s)]^n = \frac{\tilde{\varrho}_{\text{nf}}(s)}{1 - \tilde{p}_f(s)}. \quad (34)$$

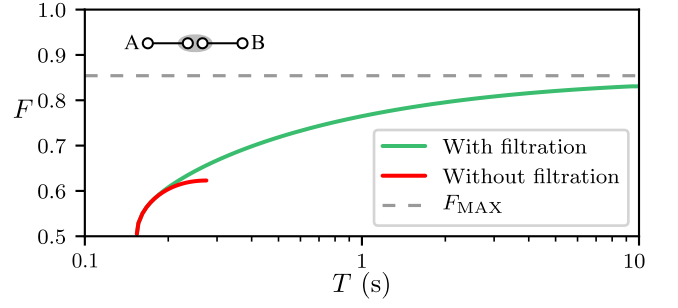


FIG. 4. Maximum fidelity $F = \langle \psi | \rho | \psi \rangle$ versus the generation time T achievable in the 1D DLCZ repeater of the nesting level I distributing the Bell state $|\psi\rangle = (|01\rangle + |10\rangle)/\sqrt{2}$ among two parties A and B, as shown in the inset. Network parameters: length $L = 300$ km, memory decay time $T_{\text{coh}} = 100$ ms, and other experimental parameters specified in [48]. Green (red) line represents optimized results obtained with (without) temporal filtering. The gray dashed line indicates fidelity F_{MAX} achievable with the network in the limit $T_{\text{coh}} = \infty$.

Merging and sum over all trajectories. The calculation of the density matrix distribution for the merged segment is identical to what was presented in Sec. IV. Therefore, one can obtain the target Laplace image $\tilde{\varrho}(s)$ by inserting $\tilde{\varrho}_{\text{prep}}(s)$ from the Eq. (34) into the Eq. (25). The average generated state and the generation time are obtained using Eqs. (1) as usual:

$$\rho = e^{\mathcal{L}t_m} \frac{\mathcal{M}\tilde{\varrho}_{\text{prep}}(0)}{\text{Tr}\{\mathcal{M}\tilde{\varrho}_{\text{prep}}(0)\}} = \frac{1}{2PP_{\text{nf}}} e^{\mathcal{L}t_m} \times \left[\frac{1 - e^{-(1-\mathcal{L}_1/\nu)\nu\tau}}{1 - \mathcal{L}_1/\nu} + \frac{1 - e^{-(1-\mathcal{L}_2/\nu)\nu\tau}}{1 - \mathcal{L}_2/\nu} \right] \rho_{\text{in}}, \quad (35)$$

$$T = \frac{1}{P} \left(t_m + \frac{3}{2\nu} + \frac{t_c + \frac{1}{2\nu}}{e^{\nu\tau} - 1} \right).$$

Here we have introduced the probability of not filtering the segment state $P_{\text{nf}} = 1 - \tilde{p}_f(0) = 1 - e^{-\nu\tau}$, the merging probability $P = \text{Tr}\{\mathcal{M}\tilde{\varrho}_{\text{prep}}(0)\}$, and the time $t_m = t_c + t_{\text{swap}}$ required for the merging including classical communication delay.

Example of a network with filtration. The striking feature of the temporal filtering protocol is that it can enable applications requiring entangled states of higher quality than the standard repeater protocol can generate given a finite memory coherence time. As presented in the Fig. 4, the temporal filtering protocol allows one to trade the generation rate $1/T$ for increase in the fidelity F of the resulting states by decreasing the filtering time τ . The red curve is obtained by only optimizing the elementary segments generation (i.e. squeezing parameter ϵ in the DLCZ protocol, see the next section) without using the temporal filtering ($\tau = \infty$). For the green curve, the filtering time τ was numerically optimized. The plot illustrates that the filtering allows the network to achieve much higher fidelities. Particularly, in the given example with memory decay time $T_{\text{coh}} = 100$ ms and network length $L = 300$ km, using filtration one can almost reach

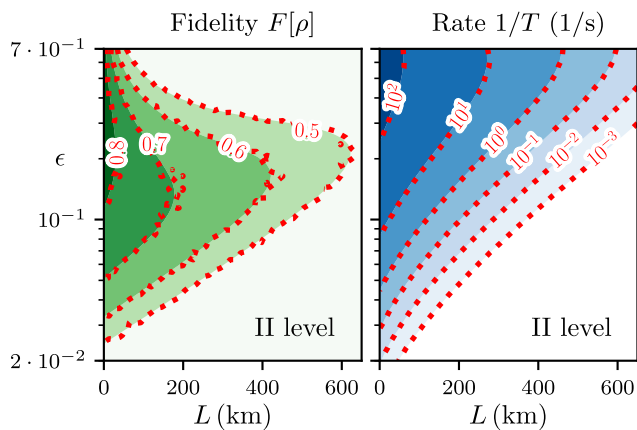


FIG. 5. Fidelity $F = \langle \psi | \rho | \psi \rangle$ (left panel) and generation rate $1/T$ (right panel) of the states generated with the 1D DLCZ repeater of the nesting level II [see Fig. 1(a)] versus network length L and squeezing parameter ϵ in generation of the elementary segments with the DLCZ protocol (see Sec. II and Appendix A). Network parameters: memory decay time $T_{\text{coh}} = 150$ ms, filtering time $\tau = 15$ ms, and other experimental parameters specified in [48]. Color contours represent data obtained by Eqs. (35), derived with the diagrammatic technique. Red dotted contours give data simulated with the Monte-Carlo (MC) method, such that each data point is obtained averaging over 4151 trajectories. Red numbers present data values for the contours.

the maximum fidelity ≈ 0.85 achievable in the limit of infinite coherence time $T_{\text{coh}} \rightarrow \infty$, while increasing the generation time to acceptable $T \approx 10$ s. On the other hand, the highest achievable fidelity without filtering is ≈ 0.62 .

As a result, with the temporal filtering protocol, the same quantum repeater network can be exploited in two regimes: high rate regime, which could be used for the secret key distribution, and high fidelity regime, which could be used for the distributed quantum computation. Notice that, in a real-world network, the switch between two regimes can be implemented in real-time by varying the filtering parameter τ .

VI. BENCHMARKING AGAINST MONTE CARLO SIMULATION

To assess the accuracy of the diagrammatic technique we compare results obtained for the 1D DLCZ repeater of the nesting level II [see Fig. 1(a)] using semi-analytical method given by Eqs. (35) with the results of the MC simulation, serving as a benchmark. Details on the MC simulation are presented in [44].

In the original one-dimensional DLCZ repeater, the elementary segments are generated as follows. Weak coherent pulses drive distant atomic ensembles (memories) resulting in entangled two-mode squeezed states of the ensembles and the out-coming photon modes

$\sum_{n=0}^{\infty} \epsilon^n |n\rangle_m^{(i)} |n\rangle_p^{(i)}$ with squeezing parameter $\epsilon \ll 1$; here the indexes m and p correspond to the memory and the photon modes and $i \in \{1, 2\}$ refers to the memory index. The two out-coming photon modes interfere with each other on a beam-splitter placed in-between of the ensembles and are measured afterward. Upon a probabilistic detection of a single photon, the state of the memories is projected onto an entangled state spanning the elementary segment length L_0 . A probabilistic swapping operation of two prepared segments is implemented by mapping the states of the neighboring memories to photon pulses, which after interfering on a beam-splitter are measured. The swapping is successful upon a single-photon detection. The details on the simulation of the elementary segments in the DLCZ scheme are given in Appendix A.

We consider experimental parameters realistic for current room-temperature atomic ensembles [21, 40]: memory decay time $T_{\text{coh}} = 150$ ms and the length of the signal pulses 10^{-4} s, which we use as t_{swap} — the time for the merging operation. The filtering time $\tau = 15$ ms is chosen such that the temporal filtering protocol significantly limits the degradation of the network memories. Other experimental parameters are specified in [48].

The simulation results are presented in the Fig 5. Color contours present the fidelity of the prepared states with respect to the target Bell state (left panel) and the average generation rate (right panel) as functions of the linear network size L and the squeezing parameter ϵ . The results of the MC simulation are given by red dotted contours and perfectly match the data obtained with the semi-analytical equations (35). Thereby, the Fig 5 verifies the accuracy of the assumptions made to develop the diagrammatic method. On the other hand, the Fig. 2 demonstrates a dramatic advantage of the proposed semi-analytical approach over the MC simulation in the calculation performance.

VII. APPLICATION FOR NETWORK OPTIMIZATION

Due to the high accuracy and the small calculation run-time, the developed technique is a powerful tool for optimization of real-world large-scale quantum networks. For example, in the Fig. 5(left panel) one can see that there is an optimal squeezing parameter ϵ which maximizes the entanglement distribution distance for the DLCZ-type repeater. Note that the Fig. 5 represents results of the simulation for a comparably small 1D network of the nesting level II because it has to be accessible for the MC simulation method.

Below we give examples of simulations of much larger networks, including a 2D network of the nesting level IV, which are made possible by the semi-analytic technique. In particular, we optimize quantum networks to maximize the rate of the secret key [49] distribution among two parties with the 1D DLCZ repeater network and among three parties with the 2D repeater network. The maximization of the secret key rate, K , is of a particular

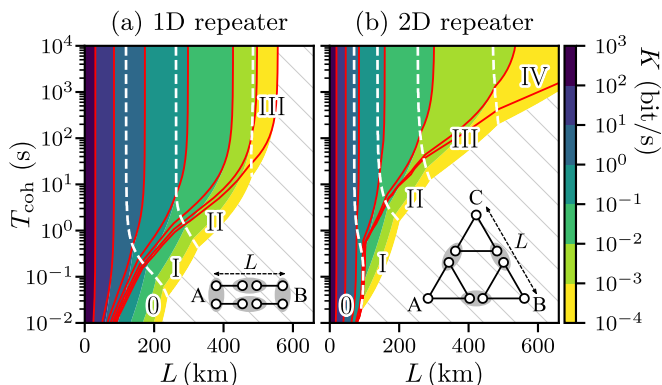


FIG. 6. The optimized rate K of the secret key distribution (a) between two parties with the 1D DLCZ repeater and (b) among three parties with the 2D repeater, obtained with the semi-analytical technique. The network schemes are sketched in the insets. Both panels display maximum rate K versus memory coherence time T_{coh} and covered distance L for the experimental parameters specified in [48]. The parameters include communication time and time for the signal detection 10^{-4} s in the merging operations, realistic for the atomic ensemble [40]. Filled color contours show results for the repeaters with the temporal filtering protocol, where white dashed contours separate areas with different optimal nesting levels numerated by the Roman numbers. Red contours indicate results of optimization for the repeaters without the temporal filtering protocol.

interest because K is a function of both, the quality and the generation rate of the prepared entangled states [see Appendix C], which, in the probabilistic repeater protocols, are traded one for another. For the demonstration, we consider the protocols with and without the temporal filtering. In the latter case, we optimize over the network nesting level and the squeezing parameter ϵ , and in the former case, the filtering time τ is added as the third parameter to optimize. The details on the simulation of the elementary segments in the 2D repeater scheme are given in Appendix A.

Figure 6 shows the maximum rate K of the secret key distribution as a function of the distribution length L and the memory decay time T_{coh} . The left panel corresponds to the 1D network and the right panel shows results for the 2D network. The plots highlight the benefits of using quantum networks with higher nesting levels to cover longer distances in the presence of the sufficiently long memory coherence time. One can also see that the temporal filtering protocol (filled color contours) provides higher key rates than the no filtering strategy (red contours) in the domain of small memory coherence times. Remarkably, this is achieved without usage of extra physical resources (e.g. multiplexing) but only with optimization of the filtering time τ . The given example of the networks optimizations illustrates the potential of the developed method for efficient designing and optimization of the real-world large-scale quantum internet.

VIII. CONCLUSION

We have presented in details and developed further the diagrammatic technique used in [44] to study 2D repeater networks. We showed examples of using the technique to evaluate the average states and the average generation times of the 1D and 2D repeater networks taking into account the communication time and incorporating the temporal filtering protocol. Compared to other analytical methods, our technique accounts for the continuous dissipative Liouville dynamics of the network quantum memories. The results obtained with the semi-analytical technique match the exact MC simulations while the required computational resources scales only linearly with the network size. We stress that the presented technique is not limited to the considered repeater models but can be applied to evaluate networks with more complex configurations realized on various experimental platforms. The diagrammatic technique is a convenient tool for investigation of new repeater protocols as it allows for precise comparison of the protocols subjected to relevant realistic imperfections. The method can be useful for designing and optimization of future real-world quantum networks.

ACKNOWLEDGMENTS

We thank C. A. Muschik and W. Dür for fruitful discussions on the quantum repeater networks. Research was sponsored by the Army Research Laboratory and was accomplished under Cooperative Agreement Number W911NF-15-2-0060. The views and conclusions contained in this document are those of the authors and should not be interpreted as representing the official policies, either expressed or implied, of the Army Research Laboratory or the U.S. Government. The U.S. Government is authorized to reproduce and distribute reprints for Government purposes notwithstanding any copyright notation herein.

Appendix A: Calculation of the elementary segments and the merging superoperator

In this section, we describe simulation of the elementary segments in the 1D and 2D quantum repeater protocols. For each protocol, we calculate the state of the elementary segment, ρ_e , success probability q to generate the segment for one attempt, and time Δt required for one generation attempt. We also calculate the merging superoperator \mathcal{M} , taking into account all relevant experimental imperfections.

1D DLCZ protocol

The scheme of the 1D DLCZ protocol [11] is shown in Fig. 7(a). Two nodes of the segment, A and B, are distributed for a distance L_0 . Each node consists of an

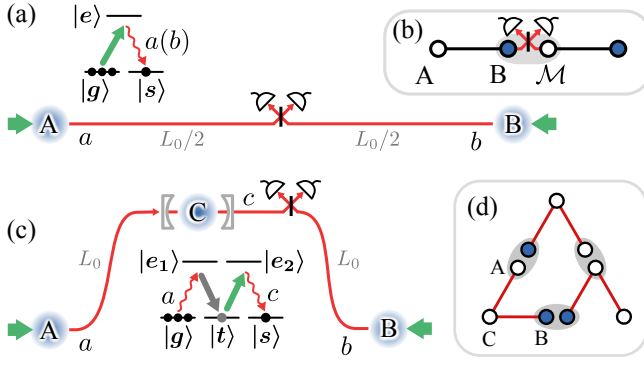


FIG. 7. Implementation schemes of the elementary segments of (a) the 1D [11] and (c) the 2D [44] repeaters. Blue gradient filled circles represent atomic ensembles with level structures depicted nearby. Bold arrows depict weak classical fields, red thin arrows represent photonic modes, half-circles represent single-photon detectors. In (c), node C is placed in a high-finesse cavity. (b) Quantum swapping operation for two prepared segments. The states of the nodes, connected by links, of the same (different) colors are correlated (anti-correlated). (d) A possible relevant position of the elementary segments of the 2D repeater for merging to nesting level I with three swapping operations depicted in (b). Red links correspond to the photonic modes as in (c).

atomic ensemble with a Λ -type level structure. Information in the ensembles is encoded in the absence or presence of a collective spin excitation, i.e., in the logical states $|0\rangle = |g_1 g_2 \dots g_N\rangle$ and $|1\rangle = \frac{1}{\sqrt{N}} \sum_{i=1}^N |g_1 g_2 \dots s_i \dots g_N\rangle$, where N is the number of emitters per ensemble, and $|g_i\rangle, |s_i\rangle$ denote the levels of the emitters. The target state of the elementary segment is $(|1_A 0_B\rangle + |0_A 1_B\rangle)/\sqrt{2}$, where subscripts refer to the corresponding ensembles. The generation of the elementary segment is probabilistic and is performed in discrete steps. At the beginning of each step, all ensembles are prepared in the states $|0\rangle$. Then, weak laser pulses drive the ensembles at nodes A and B, coupling them to the out-going photonic modes, a and b correspondingly, via off-resonant Raman transition. The resulting entangled states of the ensembles and the photonic modes are two two-mode squeezed vacuum states

$$\begin{aligned} |\Psi_{Aa(Bb)}(\epsilon_{a(b)})\rangle &= \text{sech } r_{a(b)} \\ &\times \sum_{n=0}^{\infty} (\tanh r_{a(b)})^n |n_{A(B)}\rangle |n_{a(b)}\rangle \\ &\propto \sum_{n=0}^{\infty} \epsilon_{a(b)}^n |n_{A(B)}\rangle |n_{a(b)}\rangle. \end{aligned} \quad (\text{A1})$$

Here $r_{a(b)}$ is the squeezing parameter, which is controlled by the strength of the driving laser. For simplicity, we use a notation $\epsilon_{a(b)} \equiv \tanh r_{a(b)} \in [0, 1)$.

Each of the outgoing photonic modes $i = \{a, b\}$ propagates through the length $L_0/2$ of lossy fiber. Fiber losses are represented by a loss superoperator $\mathcal{S}_{\text{loss}}^i(L_0/[2L_{\text{att}}])$,

where

$$\mathcal{S}_{\text{loss}}^i(g) \bullet = \exp \{g \mathcal{D}[a_i]\} \bullet, \quad (\text{A2})$$

with a_i the annihilation operator in the mode i , $\mathcal{D}[a] \bullet = a \bullet a^\dagger - \frac{1}{2} (a^\dagger a \bullet + \bullet a^\dagger a)$ the Lindblad superoperator, and L_{att} the attenuation length. Afterward, both photonic modes enter the station for the probabilistic swapping operation placed in-between of the two nodes, and which consists of a perfect balanced beamsplitter and two imperfect single-photon detectors. The photonic modes interfere in the beamsplitter and the outgoing modes are measured. Probabilistic detection of a single photon heralds generation of an entangled state, otherwise the generation attempt is repeated. Detectors imperfections include dark counts with rate d and a photon loss with probability f . The latter is represented by loss superoperator (A2) and the former by a dark counts superoperator

$$\mathcal{S}_{\text{dc}}^i(d) \bullet = \exp \left\{ d \mathcal{D}[a_i] + d \mathcal{D}[a_i^\dagger] \right\} \bullet.$$

A superoperator for the full swapping operation acting to two photonic modes i and j is

$$\mathcal{M}_s^{ij} \bullet = 2 \langle 1_i 0_j | \{ (\mathcal{S}_{\text{det}}^i \otimes \mathcal{S}_{\text{det}}^j) \mathcal{S}_{\text{BS}}^{ij} \bullet \} | 1_i 0_j \rangle, \quad (\text{A3})$$

where $\mathcal{S}_{\text{det}}^i = \mathcal{S}_{\text{dc}}^i(d) \mathcal{S}_{\text{loss}}^i(-\ln[1-f])$. Projection $\langle 1_i 0_j | \bullet | 1_i 0_j \rangle$ describes detection of a single photon in the photonic mode i . The prefactor 2 accounts for the possibility to detect a photon in the second photonic mode j with the corresponding projector $\langle 0_i 1_j | \bullet | 0_i 1_j \rangle$. Photon detection in different detectors give opposite phase of the resulting states which can be reduced to each other by the phase flip operation. In Eq. (A3), the superoperator for the balanced beamsplitter reads

$$\begin{aligned} \mathcal{S}_{\text{BS}}^{ij} \bullet &= U_{\text{BS}}^{ij} \bullet \left(U_{\text{BS}}^{ij} \right)^\dagger, \\ U_{\text{BS}}^{ij} &= \exp \left[\frac{\pi}{4} \left(a_i^\dagger a_j - a_i a_j^\dagger \right) \right]. \end{aligned}$$

Swapping operation (A3) is not trace-preserving, and thus is probabilistic with the success probability defined by the trace of the resulting state as $\text{Tr}\{\mathcal{M}_s^{ij} \bullet\}$.

The success/failure of the swapping operator is communicated from the central station to the nodes of the segment. Therefore, time for one generation attempt $\Delta t = v_c L_0 + t_s$ comprises time $v_c L_0/2$ required for the signals to propagate from the nodes to the swapping station, time t_s for the signal detection, and time $v_c L_0/2$ for the back communication. Here, v_c is the speed of light in the fiber and t_s is the photon pulse duration. During time Δt , memories of the nodes A and B experience decay accounted by applying the loss superoperator (A2) $\mathcal{S}_{\text{loss}}^i(\Delta t/T_{\text{coh}})$ to both memory modes $i = \{A, B\}$, where T_{coh} is the memory coherence time.

In the following, we will use the matrix-vector representations of states (A1) $|\rho_{Jj}(\epsilon_j)\rangle \equiv |\Psi_{Jj}(\epsilon_j)\rangle \langle \Psi_{Jj}(\epsilon_j)|$ with $Jj = \{Aa, Bb\}$. In the matrix-vector representations, generated state ρ_e of the 1D repeater elementary

segment reads

$$|\rho_e(\epsilon)\rangle\rangle = \mathcal{M}_s^{ab} \times \prod_{Jj=\{Aa,Bb\}} \otimes \mathcal{S}_{\text{loss}}^J \left(\frac{\Delta t}{T_{\text{coh}}} \right) \mathcal{S}_{\text{loss}}^j \left(\frac{L_0}{2L_{\text{att}}} \right) |\rho_{Jj}(\epsilon)\rangle\rangle, \quad (\text{A4})$$

where we use the optimal relation of the parameters $\epsilon_a = \epsilon_b \equiv \epsilon$. The success probability of one generation attempt is given by

$$q = \text{Tr} \{ \rho_e(\epsilon) \}.$$

Free parameter ϵ is numerically optimized for each set of the network parameters to obtain the results illustrated in Figs. 4 and 6 of the main text.

The merging operation of two prepared segments is presented in Fig. 7(b): states of two memories are read-out and directed to the swapping station, which is identical to the swapping station used in the preparation of the elementary segment. Ideally, the detection of a single photon projects the joint system into the entangled state. Taking into account inefficiency v of the read-out operation and the imperfect detectors, one can represent the merging operator acting to two modes i and j via superoperators (A2) and (A3) as

$$\mathcal{M}\bullet = \mathcal{M}_s^{ij} \mathcal{S}_{\text{loss}}^i(-\ln[1-v]) \mathcal{S}_{\text{loss}}^j(-\ln[1-v]) \bullet. \quad (\text{A5})$$

The derived merging operator \mathcal{M} is used in the numerical simulations presented in the paper.

For $\epsilon \ll 1$ only several excited states of the quantum memories and the photon modes are considerably populated. Therefore, we truncate dimensions of the bosonic modes to the Fock state $|2\rangle$, thus, taking into account the first order of the multi-excitation error.

2D repeater protocol

In the subsection, we explain the simulation of the elementary segments of the 2D repeater protocol [44]. The scheme of the elementary segment is shown in Fig. 7(c). The segment consists of three nodes A, B, and C, which are distributed in space such that the scheme has a shape of a triangle (equilateral for simplicity) with the length L_0 of the sides. Similarly to the nodes of the 1D scheme, nodes A and B contain atomic ensembles with a Λ -type level structure. Node C employs a cold atomic ensemble with a double- Λ configuration placed in a cavity with good cooperativity.

The ideal target state of the elementary segment is $|\Psi_{\text{GHZ}}\rangle = (|1_A 1_C 0_B\rangle + |0_A 0_C 1_B\rangle)/\sqrt{2}$. The generation of the elementary segment is probabilistic and is performed in discrete steps. At the beginning of each step, atoms in the ensembles are pumped into the states $|g\rangle$. Then, nodes A and B are driven with weak laser pulses to produce two-mode squeezed vacuum states (A1), similar to the 1D

repeater described above. The photonic modes propagate through the distance L_0 via lossy fiber. This is modeled by applying the loss superoperators (A2) $\mathcal{S}_{\text{loss}}^i(L_0/L_{\text{att}})$ to each photonic mode.

Mode a is directed to node C designed to implement a nonlinear gate $|1_a 0_C 0_c\rangle \rightarrow |0_a 1_C 1_c\rangle$, $|0_a 0_C 0_c\rangle \rightarrow |0_a 0_C 0_c\rangle$. Such an evolution is given by a unitary $U = \exp[\frac{\pi}{2}(aC^\dagger c^\dagger - \text{h.c.})]$, which describes swapping of the incoming photon in mode a into one outgoing photon in mode c and one excitation in the collective spin mode C of the ensemble. The inefficiency of the gate is modeled as a loss of excitation in the incoming mode a and is represented by the loss superoperator $S_{\text{loss}}^a(-\ln \eta)$ given by Eq. (A2), where η is the gate efficiency. As a result, the evolution in node B is given by the superoperator

$$\mathcal{S}_{C\bullet} = \text{Tr}_a \{ U [S_{\text{loss}}^a(-\ln \eta) \bullet] U^\dagger \},$$

where the incoming mode a is traced out since it is not measured after the interaction.

Afterward, photonic modes b and c are directed into the swapping station placed right after node C. The swapping station is similar to the one used in the 1D scheme, and is described by the superoperator (A3) \mathcal{M}_s^{ac} .

The time for one generation attempt $\Delta t = 2v_c L_0 + t_s$ consists of the time required for the propagation of the signals to the swapping station, the time t_s for the signal detection in the swapping operation, and the classical communication time. Thus, the memories in nodes A and B experience decay for time Δt and the memory in node C decays for time $T_C = v_c L_0 + t_s/T_{\text{coh}}$. The resulted state of the elementary segment reads

$$|\rho_e(\epsilon_a, \epsilon_b)\rangle\rangle = \mathcal{M}_s^{ac} \mathcal{S}_{\text{loss}}^C \left(\frac{T_C}{T_{\text{coh}}} \right) \mathcal{S}_C \times \prod_{Jj=\{Aa,Bb\}} \mathcal{S}_{\text{loss}}^J \left(\frac{\Delta t}{T_{\text{coh}}} \right) \mathcal{S}_{\text{loss}}^j \left(\frac{L_0}{2L_{\text{att}}} \right) |\rho_{Jj}(\epsilon_j)\rangle\rangle \otimes |0_C 0_c\rangle\rangle.$$

The success probabilities for one generation attempt is

$$q = \text{Tr} \{ \rho(\epsilon_a, \epsilon_b) \}.$$

Free parameters $\epsilon_{a(b)}$ are numerically optimized for each set of the network parameters to obtain the results illustrated in Fig. 6 of the main text.

Fig. 7(d) presents an example of a possible relative orientation of three elementary segments in the 2D network. This configuration is used for numerical analysis of the 2D repeater shown in Fig. 2. For simulations of both, 1D and 2D repeaters, we truncate the Hilbert space of the bosonic modes up to the Fock state $|2\rangle$.

Appendix B: Full simulation of the 2D repeater

In the following section, we use the diagrammatic technique to describe the two-dimensional (2D) repeater [44]

presented in Fig. 1(b). Here we develop further the results of Subsec. III C of the main text by incorporating the communication time and the temporal filtering protocol presented, correspondingly, in Sections IV and V of the main text for the 1D repeater.

Unlike the temporal filtering protocol for the 1D repeater, the 2D repeater version exploits two filtering times: τ_1 – time, after which the state of the first prepared segment i is discarded; and τ_2 – time, after which we discard the state resulted from the merging of the segments i and j . First, we can reuse diagram (28) of the main text to represent the successful generation of two segments, i and j , with no time filtering as

$$\varrho_{\text{nf},k}^{(1)}(t) = \left. \begin{array}{c} \text{---} \\ | \quad | \quad | \\ \text{---} \end{array} \right|, \quad t$$

such that the third segment, k , is unprepared. In the Laplace domain the extra bar results in a frequency shift of the Laplace image (29) by ν

$$\tilde{\varrho}_{\text{nf},k}^{(1)}(s) = \sum_{ij \neq k} \left(1 - e^{-(s' - \mathcal{L}_i)\tau} \right) \times \frac{\nu^2}{(s' - \mathcal{L}_i)(s' + \nu)} \rho_{\text{in}} \Big|_{s'=s+2\nu}.$$

Similarly, the probability distribution for all possible events of the segments filtration can be obtained by adding a bar to the diagram (30) and summing over filtration of each of three segments

$$\sum_i \left. \begin{array}{c} \text{---} \\ \tau_1 \downarrow \\ | \quad | \quad | \\ \text{---} \end{array} \right| \equiv \left. \begin{array}{c} \text{---} \\ | \quad | \quad | \\ \text{---} \end{array} \right|, \quad t$$

The Laplace image of this diagram is

$$\tilde{p}_{\text{f}}^{(1)}(s) = 3e^{-s(\tau_1+t_e)} \frac{\nu e^{-2\nu\tau}}{s+3\nu}.$$

All possible trajectories for preparation segments i and j are represented as

$$\varrho_{\text{prep},k}^{(1)}(t) = \left. \begin{array}{c} \text{---} \\ | \quad | \quad | \\ \text{---} \end{array} \right| + t_0 \left. \begin{array}{c} \text{---} \\ | \quad | \quad | \\ \text{---} \end{array} \right| + t_1 \left. \begin{array}{c} \text{---} \\ | \quad | \quad | \\ \text{---} \end{array} \right| + \dots,$$

with the Laplace image

$$\tilde{\varrho}_{\text{prep},k}^{(1)}(s) \equiv \frac{\tilde{\varrho}_{\text{nf},k}^{(1)}(s)}{1 - \tilde{p}_{\text{f}}^{(1)}(s)}.$$

We denote the successful attempt of merging of prepared segments i and j with unprepared segment k as

$$t_m \left. \begin{array}{c} \text{---} \\ | \quad | \quad | \\ \text{---} \end{array} \right| = \Theta(t - t_m) e^{-\mathcal{L}_{ij}t_m} \mathcal{M}_k \varrho_{\text{prep},k}^{(1)}(t), \quad (\text{B1})$$

where the superoperator \mathcal{L}_{ij} describes degradation of the resulted state for the time t_m required by the merging. All possible variants of the unsuccessful merging attempts are denoted as

$$\left. \begin{array}{c} \text{---} \\ | \quad | \quad | \\ \text{---} \end{array} \right| = \Theta(t - t_m) \text{Tr} \left\{ \sum_k (\mathcal{I} - \mathcal{M}_k) \varrho_{\text{prep},k}^{(1)}(t) \right\}, \quad (\text{B2})$$

where $k \in \{1, 2, 3\}$. Then, the density matrix distribution for generation of two segments is the following sum of trajectories

$$\varrho_k^{(2)}(t) = \left. \begin{array}{c} \text{---} \\ | \quad | \quad | \\ \text{---} \end{array} \right| + t_0 \left. \begin{array}{c} \text{---} \\ | \quad | \quad | \\ \text{---} \end{array} \right| + t_1 \left. \begin{array}{c} \text{---} \\ | \quad | \quad | \\ \text{---} \end{array} \right| + \dots \equiv \left. \begin{array}{c} \text{---} \\ | \quad | \quad | \\ \text{---} \end{array} \right|, \quad t$$

with the Laplace image obtained using Eqs. (B1), (B2)

$$\tilde{\varrho}_k^{(2)}(s) = \frac{e^{-\mathcal{L}_{ij}t_m} \mathcal{M}_k \tilde{\varrho}_{\text{prep},k}^{(1)}(s)}{e^{st_m} - \text{Tr} \left\{ \sum_k (\mathcal{I} - \mathcal{M}_k) \tilde{\varrho}_{\text{prep},k}^{(1)}(s) \right\}}.$$

Generation of the third segment k within the time period τ_2 after the merging of segments i and j is represented as

$$\begin{aligned} \varrho_{\text{nf},k}^{(2)}(t) &= t_0 \left. \begin{array}{c} \text{---} \\ | \quad | \quad | \\ \text{---} \end{array} \right|_{\tau_2} + \left. \begin{array}{c} \text{---} \\ | \quad | \quad | \\ \text{---} \end{array} \right|_{\tau_2} \\ &= \left[\Theta(\tau_2 - t) \int_0^t \bullet dt_0 + \Theta(t - \tau_2) \bullet \int_{t-\tau_2}^t dt_0 \right] \\ &\quad \times p_k(t - t_0) e^{\mathcal{L}_{ij}(t-t_0)} \varrho_k^{(2)}(t_0), \end{aligned}$$

with the Laplace image

$$\tilde{\varrho}_{\text{nf},k}^{(2)}(s) = \left(1 - e^{-(s+\nu-\mathcal{L}_{ij})\tau_2} \right) \frac{\nu}{s+\nu-\mathcal{L}_{ij}} \tilde{\varrho}_k^{(2)}(s).$$

All variants for the filtration of the merged state are represented as

$$\begin{aligned}
p_f^{(2)}(t) &= \sum_k \left[\begin{array}{c} \overbrace{\uparrow} \\ \vdots \\ \tau_2 \\ \overbrace{\downarrow} \end{array} t \right] \\
&= \Theta(t - \tau_2 - t_c) \sum_k e^{-\nu_k \tau_2} \text{Tr} \left\{ \varrho_k^{(2)}(t - \tau_2 - t_c) \right\},
\end{aligned}$$

with the Laplace image

$$\tilde{p}_f^{(2)}(s) = e^{-s(\tau_2 + t_c)} \sum_k e^{-\nu_k \tau_2} \text{Tr} \left\{ \varrho_k^{(2)}(s) \right\}.$$

Summing up the trajectories for the eventual successful generation of the third segment we again obtain the infinite series, with the Laplace image which converges to

$$\tilde{\varrho}_{\text{prep},k}^{(2)}(s) \equiv \frac{\tilde{\varrho}_{\text{nf},k}^{(2)}(s)}{1 - \tilde{p}_f^{(2)}(s)}.$$

The successful, last, merging attempt of the third segment k with the rest of the state is represented as

$$\Theta(t - t_m) e^{\mathcal{L}t_m} \sum_k \tilde{\mathcal{M}}_k \varrho_{\text{prep},k}^{(2)}(t),$$

with \mathcal{L} the superoperator describing degradation of the final state during the time required by the merging. All possible unsuccessful merging attempts are represented by

$$\Theta(t - t_m) \sum_k \text{Tr} \left\{ \left(\mathcal{I} - \tilde{\mathcal{M}}_k \right) \varrho_{\text{prep},k}^{(2)}(t) \right\}.$$

Finally, in the Laplace domain, the density matrix distribution describing the result of merging of three segments of the 2D network reads

$$\tilde{\varrho}(s) = \frac{e^{\mathcal{L}t_m} \sum_k \tilde{\mathcal{M}}_k \tilde{\varrho}_{\text{prep},k}^{(2)}(s)}{e^{st_m} - \sum_k \text{Tr} \left\{ \left(\mathcal{I} - \tilde{\mathcal{M}}_k \right) \tilde{\varrho}_{\text{prep},k}^{(2)}(s) \right\}}. \quad (\text{B3})$$

The resulting Eq. (B3) allows us to find the average state and the generation time of the larger segment as described in the main text. Repeating this procedure recursively, we can simulate the 2D network of arbitrary nesting level depth. The results of the simulation are presented the Figs. (2), and (6) of the main text.

Appendix C: Secret key rate

In the section, we review the formula for the rate of the N -partite secret key [49] generated out of N -partite entangled state. The ideal state for the generation of the secret key among N parties, A and B_i , with $i = 1, \dots, N - 1$, is the distributed N -qubit GHZ

state $|\text{GHZ}\rangle = (|0\rangle_{\text{logic}}^{\otimes N} + |1\rangle_{\text{logic}}^{\otimes N})/\sqrt{2}$, encoded in the logical Hilbert space. To obtain the key, parties make ‘‘first type’’ or the ‘‘second type’’ measurement over the qubits. The first type measurement is performed in the Z -basis $\{|0\rangle, |1\rangle\}_{\text{logic}}$, and the second type measurement in X -basis $\{1/\sqrt{2}(|0\rangle \pm |1\rangle)_{\text{logic}}\}$ or Y -basis $\{1/\sqrt{2}(|0\rangle \mp i|1\rangle)_{\text{logic}}\}$ chosen randomly. The measurements of the second type allow calculation of errors, potentially introduced by the eavesdropper. Based on the measured errors, parties can reduce the length of the key by ‘‘erasing’’ the information that the eavesdropper could have obtained to make the key completely secure. According to [50] measurements of the second type could be done much less frequently than of the first, increasing the key distribution rate. At the end of the ‘‘erasing’’ step, all parties either have the unconditionally secure key or nothing, depending on the distributed state quality.

Let us consider a quantum network which can generate N -partite state ρ for the average time T . Information in the state is encoded in a logical subspace $\{|0\rangle_{\text{logic}}, |1\rangle_{\text{logic}}\}$. According to Ref. [51], without loss of security one can discard all states that are out of the logical subspace. We denote the projector to the logical subspace as Π . The probability to find the network in the projected state, $\rho_{\Pi} \propto \Pi \rho \Pi$, is $P_{\Pi} = \text{Tr} \{\Pi \rho \Pi\}$. Then the secret key rate could be calculated as

$$R = r_{\infty}(\rho_{\Pi}) \frac{1}{T} P_{\Pi},$$

where $r_{\infty}(\rho_{\Pi})$ is the secret fraction, i.e., the ratio of the number of secret bits and the number of shared states ρ_{Π} in the limit of the infinitely long key.

To derive $r_{\infty}(\rho_{\Pi})$, in Ref. [49], a depolarization procedure is introduced, which could be applied locally to the N -qubit state, depolarizing it to a state diagonal in the GHZ basis

$$|\psi_j^{\pm}\rangle = \frac{1}{\sqrt{2}} (|0\rangle |j\rangle \pm |1\rangle |\bar{j}\rangle)_{\text{logic}}.$$

In the state above, the first qubit belongs to the party A , j takes the values $0, \dots, 2^{N-1} - 1$ in binary notation, and \bar{j} denotes the binary negation of j ; i.e., for example if $j = 01101$ then $\bar{j} = 10010$. Depolarized version of state ρ_{Π} reads

$$\begin{aligned}
\rho_{\Pi}^{\text{dep}} &= \lambda_0^+ |\psi_0^+\rangle \langle \psi_0^+| + \lambda_0^- |\psi_0^-\rangle \langle \psi_0^-| \\
&\quad + \sum_{j=1}^{2^{N-1}-1} \lambda_j (|\psi_j^+\rangle \langle \psi_j^+| + |\psi_j^-\rangle \langle \psi_j^-|), \quad (\text{C1})
\end{aligned}$$

where all coefficients could be found as $\langle \psi_j^{\pm} | \rho_{\Pi} | \psi_j^{\pm} \rangle$.

From decomposition (C1) one can find the probability that the Z -measurement outcome of the party B_i disagrees with the one of the party A

$$Q_{AB_i} = 2 \sum_{j=1}^j \lambda_j,$$

where $j^{(i)}$ denotes the i^{th} bit of j . The probabilities that at least one party B_i obtains a different outcome in the Z -bases than the party A could be found as

$$Q_Z = 1 - \lambda_0^+ - \lambda_0^-.$$

The probability that the X -measurement gives a result incompatible with the noiseless state is

$$Q_X = \frac{1 - \lambda_0^+ + \lambda_0^-}{2}.$$

Finally, the secret fraction found un [49] as

$$\begin{aligned} r_\infty(\rho_\Pi) &= \left(1 - \frac{Q_Z}{2} - Q_X\right) \log_2 \left(1 - \frac{Q_Z}{2} - Q_X\right) \\ &\quad + \left(Q_X - \frac{Q_Z}{2}\right) \log_2 \left(Q_X - \frac{Q_Z}{2}\right) \\ &+ (1 - Q_Z) [1 - \log_2(1 - Q_Z)] - h \left(\max_{1 \leq i \leq N-1} Q_{AB_i} \right), \end{aligned}$$

with $h(p) = -p \log_2 p - (1-p) \log_2(1-p)$ the binary Shannon entropy.

For example, Fig. 6(a) of the main text presents secret key distribution between two parties A and B with two parallel DLCZ links, each of which has the target state $(|0_A 1_B\rangle + |1_A 0_B\rangle)/\sqrt{2}$ in the excitation encoding. The logical Z -basis for the measurement of two local pares of the qubits at each party side is $\{|0\rangle, |1\rangle\}_{\text{logic}}^A = \{|10\rangle_A, |01\rangle_A\}$ for the party A and $\{|0\rangle, |1\rangle\}_{\text{logic}}^B = \{|01\rangle_B, |10\rangle_B\}$ for the party B, were the first and the second qubits of the states belong to the first and the second links correspondingly. All multiple-click or no-click events are discarded.

The tripartite key generation among parties A, B and C is shown in Fig. 6(b). The target state distributed with the 2D network is $(|0_A 0_B 1_C\rangle + |1_A 1_B 0_C\rangle)/\sqrt{2}$ in the excitation encoding. The logical basis for the parties A and B is $\{|0\rangle, |1\rangle\}_{\text{logic}}^{A(B)} = \{|0\rangle_{A(B)}, |1\rangle_{A(B)}\}$ and for the party C is $\{|0\rangle, |1\rangle\}_{\text{logic}}^C = \{|1\rangle_C, |0\rangle_C\}$.

In the paper, we consider the measurement of the memories states with the imperfect photodetectors. Therefore, we apply the loss superoperator (A2) $\mathcal{S}_{\text{loss}}(-\ln[1-v])$, with v the detectors inefficiency, to each memory of the generated state before the secret key is calculated.

-
- [1] S. Wehner, D. Elkouss, and R. Hanson, *Science* **362** (2018), 10.1126/science.aam9288.
- [2] D. Bruß and N. Lütkenhaus, *AAECC* **10**, 383 (2000).
- [3] R. Beals, S. Brierley, O. Gray, A. W. Harrow, S. Kutin, N. Linden, D. Shepherd, and M. Stather, *Proc Math Phys Eng Sci* **469** (2013).
- [4] P. Komar, E. M. Kessler, M. Bishof, L. Jiang, A. S. Sørensen, J. Ye, and M. D. Lukin, *Nat Phys* **10**, 582 (2014).
- [5] Z. Eldredge, M. Foss-Feig, J. A. Gross, S. L. Rolston, and A. V. Gorshkov, *Phys. Rev. A* **97**, 042337 (2018).
- [6] T. J. Proctor, P. A. Knott, and J. A. Dunningham, *Phys. Rev. Lett.* **120**, 080501 (2018).
- [7] W. Ge, K. Jacobs, Z. Eldredge, A. V. Gorshkov, and M. Foss-Feig, *Phys. Rev. Lett.* **121**, 043604 (2018).
- [8] H. J. Briegel, W. Dür, J. I. Cirac, and P. Zoller, *Physical Review Letters* **81**, 5932 (1998), arXiv:9803056 [quant-ph].
- [9] N. Sangouard, C. Simon, H. de Riedmatten, and N. Gisin, *Rev. Mod. Phys.* **83**, 33 (2011).
- [10] Bennett, Brassard, Crépeau, Jozsa, Peres, and Wootters, *Physical review letters* **70**, 1895 (1993), arXiv:9710013 [quant-ph].
- [11] L.-M. Duan, M. Lukin, I. Cirac, and P. Zoller, *Nature* **414**, 413 (2001), arXiv:0105105 [quant-ph].
- [12] S.-K. Liao, W.-Q. Cai, J. Handsteiner, B. Liu, J. Yin, L. Zhang, D. Rauch, M. Fink, J.-G. Ren, W.-Y. Liu, Y. Li, Q. Shen, Y. Cao, F.-Z. Li, J.-F. Wang, Y.-M. Huang, L. Deng, T. Xi, L. Ma, T. Hu, L. Li, N.-L. Liu, F. Koidl, P. Wang, Y.-A. Chen, X.-B. Wang, M. Steindorfer, G. Kirchner, C.-Y. Lu, R. Shu, R. Ursin, T. Scheidl, C.-Z. Peng, J.-Y. Wang, A. Zeilinger, and J.-W. Pan, *Phys. Rev. Lett.* **120**, 030501 (2018).
- [13] P. C. Humphreys, N. Kalb, J. P. J. Morits, R. N. Schouten, R. F. L. Vermeulen, D. J. Twitchen, M. Markham, and R. Hanson, *Nature* **558**, 268 (2018).
- [14] S. Wengerowsky, S. K. Joshi, F. Steinlechner, J. R. Zichi, S. M. Dobrovolskiy, R. van der Molen, J. W. N. Los, V. Zwiller, M. A. M. Versteegh, A. Mura, D. Calonico, M. Inguscio, H. Hübel, L. Bo, T. Scheidl, A. Zeilinger, A. Xuereb, and R. Ursin, *Proceedings of the National Academy of Sciences* **116**, 6684 (2019).
- [15] M. Zhong, M. P. Hedges, R. L. Ahlefeldt, J. G. Bartholomew, S. E. Beavan, S. M. Wittig, J. J. Longdell, and M. J. Sellars, *Nature* **517**, 177 (2015), arXiv:1411.6758.
- [16] J. Borregaard, M. Zugenmaier, J. M. Petersen, H. Shen, G. Vasilakis, K. Jensen, E. S. Polzik, and A. S. Sørensen, *Nature Communications* **7**, 11356 (2016), arXiv:arXiv:1011.1669v3.
- [17] Y. Wang, M. Um, J. Zhang, S. An, M. Lyu, J.-N. Zhang, L. M. Duan, D. Yum, and K. Kim, *Nature Photonics* **11**, 646 (2017).
- [18] Y. F. Pu, N. Jiang, W. Chang, H. X. Yang, C. Li, and L. M. Duan, *Nature Communications* **8**, 1 (2017), arXiv:1707.07267.
- [19] T. Zhong, J. M. Kindem, J. G. Bartholomew, J. Rochman, I. Craiciu, E. Miyazono, M. Bettinelli, E. Cavalli, V. Verma, S. W. Nam, F. Marsili, M. D. Shaw, A. D. Beyer, and A. Faraon, *Science* **357**, 1392 (2017).
- [20] C. Laplane, P. Jobez, J. Etesse, N. Gisin, and M. Afzelius, *Physical Review Letters* **118**, 1 (2017), arXiv:1705.03679.
- [21] O. Katz and O. Firstenberg, *Nature Communications* **9**, 1 (2018), arXiv:1710.06844.

- [22] J.-P. Dou, A.-I. Yang, M.-Y. Du, D. Lao, J. Gao, L.-F. Qiao, H. Li, X.-L. Pang, Z. Feng, H. Tang, and X.-M. Jin, *Communications Physics* **1**, 55 (2018), arXiv:1704.06309.
- [23] M. Körber, O. Morin, S. Langenfeld, A. Neuzner, S. Ritter, and G. Rempe, *Nature Photonics* **12**, 18 (2018).
- [24] C. E. Bradley, J. Randall, M. H. Abobeih, R. C. Berrevoets, M. J. Degen, M. A. Bakker, M. Markham, D. J. Twitchen, and T. H. Taminiau, *Phys. Rev. X* **9**, 031045 (2019).
- [25] Y. Wang, J. Li, S. Zhang, K. Su, Y. Zhou, K. Liao, S. Du, H. Yan, and S.-L. Zhu, *Nature Photonics* **13**, 346 (2019).
- [26] A. Seri, A. Lenhard, D. Rieländer, M. Gündogan, P. M. Ledingham, M. Mazzera, and H. de Riedmatten, *Physical Review X* **7**, 1 (2017).
- [27] A. Dréau, A. Tchekhovateva, A. E. Mahdaoui, C. Bonato, and R. Hanson, *Physical Review Applied* **9**, 1 (2018).
- [28] M. Rancic, M. P. Hedges, R. L. Ahlefeldt, and M. J. Sellars, *Nature Physics* **14**, 50 (2018).
- [29] M. F. Askarani, M. L. G. Puigibert, T. Lutz, V. B. Verma, M. D. Shaw, S. W. Nam, N. Sinclair, D. Oblak, and W. Tittel, *Physical Review Applied* **11**, 1 (2019).
- [30] V. Krutyanskiy, M. Meraner, J. Schupp, V. Krcmarsky, H. Hainzer, and B. P. Lanyon, *npj Quantum Information* **5**, 72 (2019), arXiv:1901.06317.
- [31] T. van Leent, M. Bock, R. Garthoff, K. Redeker, W. Zhang, T. Bauer, W. Rosenfeld, C. Becher, and H. Weinfurter, *Phys. Rev. Lett.* **124**, 010510 (2020).
- [32] X. Su, C. Tian, X. Deng, Q. Li, C. Xie, and K. Peng, *Physical Review Letters* **117**, 1 (2016).
- [33] Q.-C. Sun, Y.-F. Jiang, Y.-L. Mao, L.-X. You, W. Zhang, W.-J. Zhang, X. Jiang, T.-Y. Chen, H. Li, Y.-D. Huang, X.-F. Chen, Z. Wang, J. Fan, Q. Zhang, and J.-W. Pan, *Optica* **4**, 1214 (2017).
- [34] Y. Tsujimoto, M. Tanaka, N. Iwasaki, R. Ikuta, S. Miki, T. Yamashita, H. Terai, T. Yamamoto, M. Koashi, and N. Imoto, *Scientific Reports* **8**, 1 (2018).
- [35] M. Zopf, R. Keil, Y. Chen, J. Yang, D. Chen, F. Ding, and O. G. Schmidt, *Phys. Rev. Lett.* **123**, 160502 (2019).
- [36] O. A. Collins, S. D. Jenkins, A. Kuzmich, and T. A. B. Kennedy, *Physical Review Letters* **98**, 060502 (2007), arXiv:0610036 [quant-ph].
- [37] J. B. Brask and A. S. Sørensen, *Physical Review A* **78**, 012350 (2008), arXiv:0803.2069.
- [38] E. Shchukin, F. Schmidt, and P. van Loock, *Phys. Rev. A* **100**, 032322 (2019).
- [39] S. Santra, L. Jiang, and V. S. Malinovsky, *Quantum Science and Technology* **4**, 025010 (2019).
- [40] J. Borregaard, P. Kómár, E. M. Kessler, M. D. Lukin, and A. S. Sørensen, *Phys. Rev. A* **92**, 012307 (2015).
- [41] C. Jones, D. Kim, M. T. Rakher, P. G. Kwiat, and T. D. Ladd, *New Journal of Physics* **18**, 083015 (2016).
- [42] T. Matsuo, T. Satoh, S. Nagayama, and R. Van Meter, *Physical Review A* **97**, 062328 (2018), arXiv:1710.06214.
- [43] A. Dahlberg, M. Skrzypczyk, T. Coopmans, L. Wubben, F. Rozpundinedek, M. Pompili, A. Stolk, P. Pawelczak, R. Knegjens, J. de Oliveira Filho, R. Hanson, and S. Wehner, in *Proceedings of the ACM Special Interest Group on Data Communication*, SIGCOMM '19 (Association for Computing Machinery, New York, NY, USA, 2019) pp. 159–173.
- [44] V. V. Kuzmin, D. V. Vasilyev, N. Sangouard, W. Dür, and C. A. Muschik, *npj Quantum Information* **5**, 115 (2019).
- [45] The plot shows the computation time using one core of Apple MacBook Air with a 22-nm 1.7 GHz Intel Core i7 processor (4650U).
- [46] The decay of the corresponding quantum memories is described by the Master Equation $\dot{\rho}_i = \mathcal{L}_i \rho_i$ with the Lindblad superoperator \mathcal{L}_i :
- $$\mathcal{L}_i \bullet = T_{\text{coh}}^{-1} \sum_k \left[c_k^{(i)} \bullet c_k^{(i)\dagger} - \frac{1}{2} \{ c_k^{(i)\dagger} c_k^{(i)}, \bullet \}_+ \right],$$
- where $c_k^{(i)}$ is the jump operator describing a desired model of decoherence for the k^{th} quantum memory of the segment i , the black dot is a placeholder for the density matrix, and $\{ \dots \}_+$ corresponds to the anticommutator.
- [47] B. C. Jacobs, T. B. Pittman, and J. D. Franson, *Physical Review A* **66**, 052307 (2002), arXiv:0204097 [quant-ph].
- [48] The following parameters were used: detection inefficiency $f = 0.02$, read-out inefficiencies $v = 0.02$, fiber attenuation length $L_{\text{att}} = 22\text{km}$, gate efficiency (for the 2D repeater only) $\eta = 0.6$, signal length $l = 10^{-4}\text{s}$, and dark count probability in the signal measurement operation $d = 10\text{Hz} \cdot 10^{-4}\text{s} = 0.001$.
- [49] M. Epping, H. Kampermann, C. Macchiavello, and D. Bruß, *New Journal of Physics* **19**, 093012 (2017), arXiv:1612.05585.
- [50] H.-K. Lo, H. Chau, and M. Ardehali, *Journal of Cryptology* **18**, 133 (2005), arXiv:0011056v3 [arXiv:quant-ph].
- [51] T. Moroder, M. Curty, and N. Lütkenhaus, *New Journal of Physics* **11** (2009), 10.1088/1367-2630/11/4/045008, arXiv:0811.0027.